Analysis of the near-wall flow field in shock-cooling-film interaction for varying shock impingement positions

Pascal Marquardt

Institute of Aerodynamics
RWTH Aachen University
52062 Aachen, Germany
p.marquardt@aia.rwth-aachen.de

Michael Klaas

Institute of Aerodynamics
RWTH Aachen University
52062 Aachen, Germany
m.klaas@aia.rwth-aachen.de

Wolfgang Schröder

Institute of Aerodynamics
RWTH Aachen University
52062 Aachen, Germany
office@aia.rwth-aachen.de

ABSTRACT

A supersonic film-cooling configuration with shock interaction is investigated experimentally by means of high-speed particle-image velocimetry. A laminar cooling film is injected at an injection Mach number of $Ma_i = 1.8$ beneath a turbulent boundary layer at a freestream Mach number of $Ma_\infty = 2.45$. A flow deflection of $\beta = 8$ deg generates a shock wave which impinges upon the cooling film at different streamwise positions in the potential-core or the wall-jet region. The influence of the impingement position of the incident shock on the cooling film is analyzed by time-averaged velocity fields and Reynolds shear stress distributions. The results show severe shock-induced flow separation. Shock impingement in the wall-jet region leads to a significantly larger separation bubble compared to shock impingement in the potential-core region. The shock interaction causes intense turbulent mixing between the outer flow and the cooling film downstream of the impingement position. The Reynolds shear stress is increased by a factor of 6 and by a factor of 8 for shock impingement in the potential-core region and in the wall-jet region compared the undisturbed reference case.

Introduction

In supersonic applications with high thermal loads, e.g., scramjet combustors, supersonic film cooling through two-dimensional slots is a promising concept to cool surfaces (Juhany & Hunt (1994); Konopka *et al.* (2012, 2013)). However, shocks which interfere with the cooling film can cause a locally reduced cooling effectiveness. Figure 1 shows the basic structure of the flow field of a tangential film-cooling configuration that is not influenced by an impinging shock wave (Konopka *et al.* (2012)). According to Seban & Back (1962) and Juhany & Hunt (1994), the flow field can be divided into three regions. The first region is the potential-core region right downstream of the injection, which is bounded by the mixing layer that emanates from the lip and the slot-flow boundary layer. In this region, the cooling effectiveness is unity. The potential-core region ends where the mixing layer and the slot flow boundary layer merge and form the so-called wall-jet region that is characterized by intense mixing. Further downstream, the flow relaxes to an undisturbed turbulent boundary layer. Consequently, this region is called boundary-layer region.

To understand the impact of the shock impingement position on the overall shear flow and the turbulent structures and as such on the heat transfer, the interaction of an oblique shock with a supersonic cooling film flow either in the potential-core region or the wall-jet region is experimentally investigated. The cooling film is injected tangentially at an injection Mach number of $Ma_i = 1.8$ through a two-dimensional slot nozzle into a supersonic turbulent boundary layer with a freestream Mach number of $Ma_\infty = 2.45$. An oblique shock is generated by a flow deflection of $\beta = 8$ deg and impinges upon the cooling film at two streamwise positions, i.e., 17 and 40 nozzle heights downstream of the injection. The flow field is investigated in detail using high-speed particle-image velocimetry (PIV) measurements. The mean flow field as well as turbulence statistics are analyzed and compared for the cases with and without shock interaction.

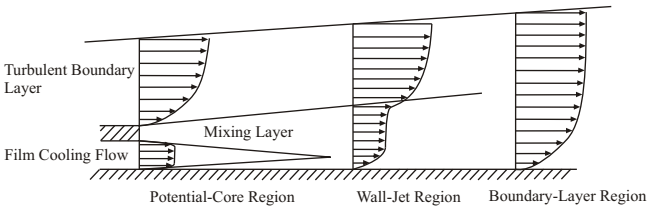

Figure 1. Flow schematic with velocity profiles indicating the three distinct flow regions (Seban & Back (1962); Juhany & Hunt (1994)) in a tangential film-cooling configuration (Konopka *et al.* (2012)).

Experimental setup: wind tunnel and model

All experiments have been conducted in the trisonic wind tunnel of the Institute of Aerodynamics of the RWTH Aachen University. This tunnel is an intermittent working vacuum storage tunnel that provides flows at Mach numbers ranging from 0.3 to 4.0. The unit Reynolds number varies between $6 \cdot 10^6$ and $16 \cdot 10^6$ m^{-1} depending on the Mach number and the ambient conditions. The freestream Mach number Ma_∞ in the test section is calculated from the pressure ratio p/p_0. The static pressure p is measured via pressure taps in the test section side walls during each run of the wind tunnel. The total pressure p_0 is measured with the same transducer just before each test run. The measurement error of the pressure transducer of 0.3%FS introduces an uncertainty in the Mach number determination of $\pm 1.3\%$.

The model, mainly made of aluminum, spans across the entire

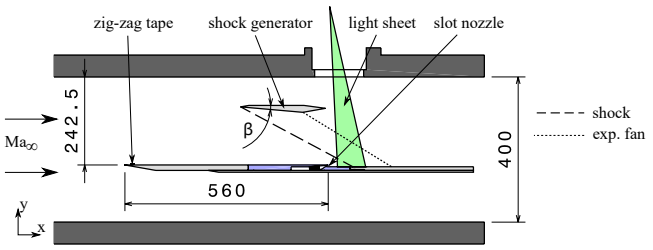

Figure 2. Dimensions of the wind tunnel model and its location in the test section.

400 mm × 400 mm test section of the wind tunnel, has an overall length of 960 mm and possesses a thickness of 20 mm. The dimensions of the model and its position in the test section are sketched in figure 2. The incoming flow is tripped by a 0.2 mm thick zigzag tape 10 mm downstream of the wedge-shaped leading edge of the model to ensure a uniform turbulent boundary layer at the position of injection. The cooling film is injected 560 mm downstream of the leading edge of the model through a 200 mm wide centered slot nozzle and develops along a 400 mm long flat plate. The oblique shock is generated by a wedge with a flow deflection angle of $\beta = 8$ deg. The expansion fan emanating from the shock generator reaches the model 87 mm downstream of the shock impingement location.

The injection flow enters the plenum chamber of the model symmetrically from both sides through rectangular ducts. Corner vanes inside the plenum chamber deflect the cooling flow by 90 deg into the main flow direction and smoothly adapt the cross-section areas between the inlets and the outlet to avoid flow separation inside the plenum. Before the flow is accelerated to the injection Mach number, it is guided through a honeycomb flow straightener with a cell size of 1.6 mm and a length of 28 mm. The static pressure and temperature of the cooling film are monitored via a pressure tap and a thermocouple downstream of the flow straightener. Upstream of the flow straightener, two struts are installed to avoid a deformation of the nozzle due to the increased pressure inside the plenum chamber. The supersonic part of the Laval nozzle is designed as a symmetric, bell-shaped nozzle with an exit height of $S = 4$ mm and a lip thickness of 1 mm. A spanwise cross section of the plenum chamber is depicted in figure 3 and the streamwise cross section is shown in figure 4.

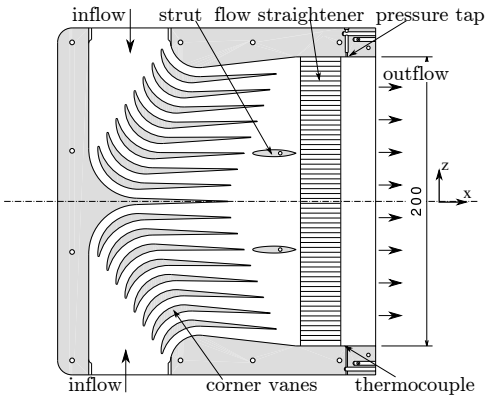

Figure 3. Spanwise cross section of the plenum chamber.

To generate a steady cooling film, the plenum chamber is supplied with a constant mass flow such that the static pressure at the nozzle outlet equals the static pressure of the freestream flow in the

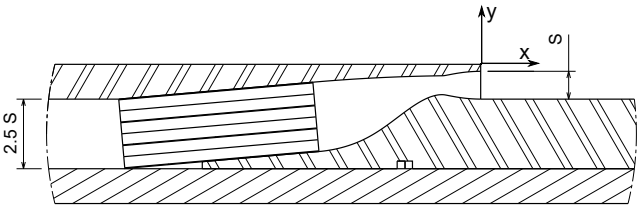

Figure 4. Streamwise cross section of the slot nozzle for an injection Mach number of $Ma_i = 1.8$.

wind tunnel test section at the point of injection. The constant mass flow is generated by a choked Venturi nozzle and a heat exchanger upstream of the Venturi nozzle controls the total temperature of the cooling fluid. Downstream of the Venturi nozzle, a part of the flow passes through two DEHS seeding generators with six Laskin nozzles each. A bypass controls the seeded flow fraction and, thus, the seeding density without changing the overall mass flow rate of the cooling-film flow. With this setup, the mass flow rate settles within 1 s to steady state with a standard deviation of 0.5% of the set mass flow rate during a test run. The standard deviation of the static pressure inside the plenum is below 0.7% and the temperature is kept constant within ±0.2 K during each measurement.

PIV setup and data evaluation

The PIV setup consists of a Quantronix Darwin Duo 527-40-M laser and a Photron Fastcam SA5 high-speed PIV camera which are synchronized by an ILA synchronizer. The light sheet enters the wind tunnel through a window in the ceiling of the test section and is positioned vertically and parallel to the flow on the centerline of the model, see figure 2. The camera is mounted at an angle of approximately 2 deg to the normal of the light sheet under Scheimpflug condition to reduce aero-optical aberrations. It is equipped with a 180 mm Tamron tele macro lens and records a field of view of 20 mm × 20 mm in the measurement plane. In the current setup, the PIV system records 1000 samples per second with a resolution of 1024×1024 px^2. To reduce the amount of laser light scattered from the model surface into the camera, the surface is highly polished. In addition to the seeding of the cooling flow, the main flow is also seeded with DEHS. The seeding in the main flow is filtered using a cyclone particle separator that reduces the mean particle diameter. The flow tracking capability of the particles has been investigated by measuring the flow over an oblique shock. The particle response time of the tracers in the main flow is $\tau_p = 2.6$ µs and the corresponding effective mean particle diameter is $d_p = 0.7$ µm. The resulting relaxation length of the particles in the freestream flow for small velocity changes is $l_p = 1.5$ mm. Accordingly, the particle response time of the seeding in the cooling flow without the cyclone separator is $\tau_{p,i} = 7.1$ µs and $d_{p,i} = 1.2$ µm. The relaxation length of the particles in the cooling-film flow is $l_{p,i} = 2.9$ mm.

Each measurement consists of 1000 snapshots recorded over 1 s. After subtraction of a background image, the particle images are preprocessed using a non-linear Gaussian blur to reduce camera noise. The image evaluation uses an iterative correlation scheme with subpixel accurate image deformation. The window size used for PIV evaluation is 48×48 px^2 with 75% overlap corresponding to a physical size of 1 mm × 1 mm. This leads to a final vector spacing of 0.25 mm. Since the surface reflections were masked in the recorded images, the first point used for PIV interrogation is at $\Delta y = 0.25$ mm off the wall. Outliers in the vector field are determined using a normalized median test resulting in a validation rate over 90% in the final dataset.

Since the field of view is approx. 20 mm × 20 mm in the current setup and the cooling-film flow evolves over a considerably

			Shock strength			Injection flow		Blowing rate
Case	Ma_∞	x_{imp}/S	β[deg]	σ[deg]	p_2/p_1	Ma_i	Re_i	$M=\rho_i u_i/\rho_\infty u_\infty$
I	2.45	-	-	-	-	1.8	$20.7\cdot10^3$	0.636
II	2.45	16.6	8	30.6	1.64	1.8	$20.7\cdot10^3$	0.636
III	2.45	39.6	8	30.6	1.64	1.8	$20.7\cdot10^3$	0.636

Table 1. Flow parameters

larger length, the results for each set of flow parameters is composed of up to 11 separate measurements along the centerplane of the model in the streamwise direction. For the case with the more downstream shock impingement position, additional measurements were performed further off the wall to account for the much larger separation region. In the results, the bounds of each measurement are indicated by thin black lines in the final vector fields.

The small field of view and the high velocities of up to 600 m/s require pulse distances of 1000 ns or less. Hence, the relatively long laser pulse width of 210 ns introduces a significant amount of particle blur in the recorded particle images. Additionally, due to slight differences in the temporal pulse shape of both laser cavities, the effective pulse distance differs up to $\pm$40 ns from the set pulse distance. To correct this systematic error, each measurement has been conducted twice, once with normal order of the laser cavities and once with reversed order of the cavities as described in detail in Marquardt *et al.* (2016*a*). With this procedure, the pulse distance error can be estimated with a typical uncertainty of $2-4$ ns, hence, the systematic error is reduced to a value less than 0.4%.

Flow parameters

In this study, a cooling-film flow with an injection Mach number of $Ma_i = 1.8$ is investigated without and with shock interaction at two shock impingement positions. The cooling film is injected beneath a turbulent boundary layer with a freestream Mach number of $Ma_\infty = 2.45 \pm 0.03$ and a Reynolds number based on the slot height S of $Re_S = (u_0 S)/v_0 = 41.6\cdot10^3 \pm 2.9\%$. The inflow boundary layer possesses a thickness of $\delta_{99}/S = 2.0$ at the point of injection. The boundary layer profiles of the mean streamwise velocity, the streamwise and wall-normal velocity fluctuations, and the Reynolds shear stress have been validated against DNS data of Pirozzoli & Bernardini (2011, 2013). A fully turbulent inflow boundary layer has been confirmed. The total temperature ratio between the cooling flow and the main flow is $T_{0,i}/T_0 = 1.00\pm0.8\%$ leading to a blowing rate of $M = (\rho_i u_i)/(\rho_0 u_0) = 0.636$ and an injection Reynolds number based on the slot height of $Re_i = (u_i S)/v_i = 20.7\cdot10^3$. The shock is generated by a flow deflection of $\beta = 8$ deg resulting in a shock angle of $\sigma = 30.6$ deg and a static pressure ratio across the shock of $p_2/p_1 = 1.64$. Three cases are considered in this study. A reference case without shock interaction (case I), and two cases with shock impingement at $x_{imp}/S = 17$ (case II) and $x_{imp}/S = 40$ (case III). The impingement position x_{imp} is determined by linear extrapolation of the oblique shock above the shear layer. The quantity x_{imp} denotes the virtual impingement position in an inviscid, unperturbed flow. The parameters of the three investigated flow configurations are summarized in table 1.

Results

To get an impression of the global structure of the flow field downstream the injection, the shock and expansion waves in the flow are visualized by means of synthetic schlieren images calculated from the normalized mean velocity divergence $-\overline{\nabla\cdot\vec{u}}\,S/u_0$. The continuity equation can be rewritten to show that $-\nabla\cdot\vec{u} = (1/\rho)\,(d\rho/dt)$, which is the relative rate of change of the density along a streamline. Although the unknown correlation term $\nabla\cdot\overline{\vec{u}'\rho'}$ is introduced by Reynolds-averaging the continuity equation, $\nabla\cdot\overline{\vec{u}}$ provides a good qualitative estimate of the shock and expansion waves in the flow field. In a two-dimensional flow, the mean velocity divergence can be derived from the 2C-PIV measurements of the in-plane velocity components $\overline{u}$ and $\overline{v}$ since $\partial\overline{w}/\partial z = 0$ for the mean out-of-plane component $\overline{w}$. Positive values of $-\overline{\nabla\cdot\vec{u}}\,S/u_0$ imply a density increase or compression, whereas negative values show expansion.

In figure 5, the synthetic schlieren image is shown for the case with shock impingement at $x_{imp}/S = 17$ (case II, Fig. 5a) and at $x_{imp}/S = 40$ (case III, Fig. 5b). The sonic line calculated under the assumption that the flow is adiabatic is superimposed in the figures. At the nozzle lip, expansion waves and recompression shocks are formed that extend into the flow field. The downward going recompression shock impinges upon the bottom wall at $x/S = 2.7$ where it is reflected off the wall.

In case II, where the shock impinges on the bottom wall at $x_{imp}/S = 17$, the reflected shock is formed around $x/S = 9$ and intersects the incident shock at $x/S = 11$ about 3.3 nozzle heights off the wall. With the shock impingement further downstream at $x_{imp}/S = 40$ (case III) the flow starts to compress upstream the shock impingement just at the beginning of the measured field of view at $x/S \approx 24$. The compression waves accumulate and form the reflected shock which passes through the incident shock at about $x/S = 31$ and 5.3 nozzle heights off the wall. In both cases, a thick subsonic layer is created which has its maximum thickness at the position of the foot of the incident shock wave, i.e., at $x/S = 12$

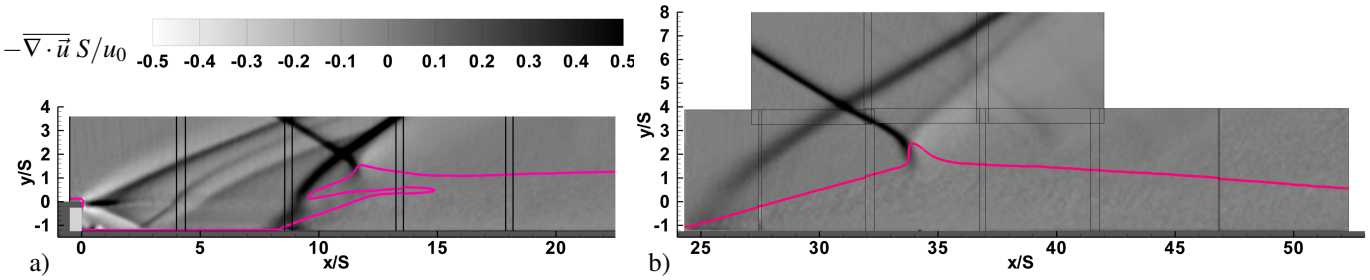

Figure 5. Synthetic schlieren image $-\overline{\nabla\cdot\vec{u}}\,S/u_0$ for case II with shock interaction at $x_{imp}/S = 17$ (a), and case III with shock interaction at $x_{imp}/S = 40$ (b). The magenta line (—) denotes the sonic line assuming adiabatic flow.

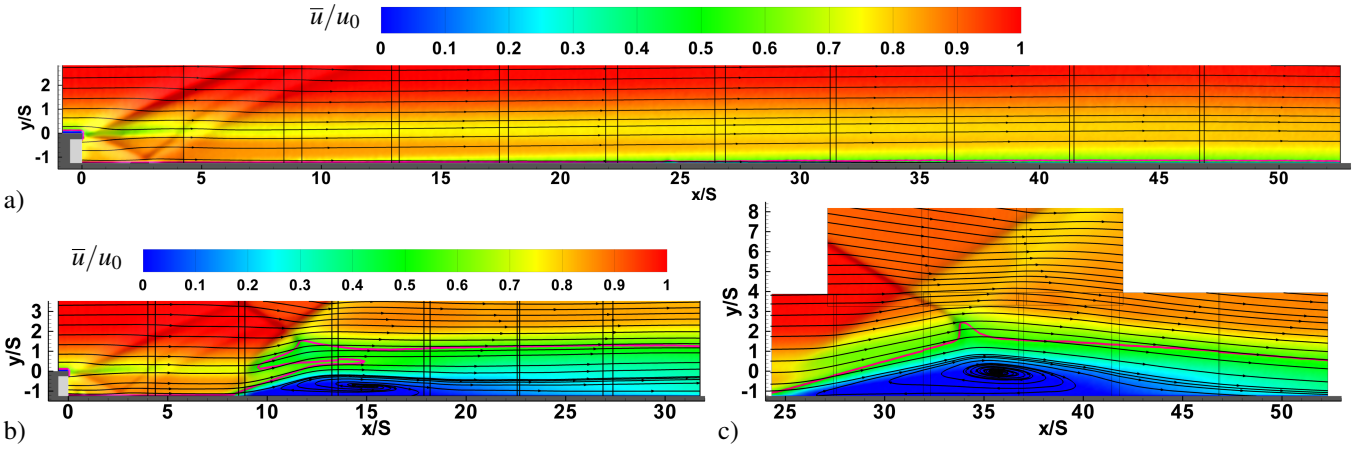

Figure 6. Contours of the normalized mean streamwise velocity $\overline{u}/u_0$ for case I without shock interaction (a), for case II with shock interaction at $x_{imp}/S = 17$ (b), and for case III with shock interaction at $x_{imp}/S = 40$. Plots (b) and (c) share the same color map. The synthetic schlieren image is superimposed to illustrate the positions of the shock and expansion waves.

(case II) and $x/S = 34$ (case III).

The contours of the normalized mean streamwise velocity $\overline{u}/u_0$ for all cases are shown in figure 6. The shading of the synthetic schlieren image is overlaid to visualize the shock positions. Figure 6a shows the undisturbed development of the flow without shock interaction as a reference case. With shock impingement (Fig. 6b and Fig. 6c), significant shock induced flow separation can be observed. However, the extent of the separation bubble differs. The size of the separation bubble is determined by identifying the positions of zero mean streamwise velocity close to the wall. For case II, this leads to a separation point at $x_{sep} = 9.4$, reattachment at $x/S = 18$, and, hence, a length of the separation bubble of $\Delta x/S = 8.6$. Shock interaction at $x_{imp}/S = 40$ creates a considerably larger separation bubble with a length of $\Delta x/S = 14.6$ with a position of the separation point at $x_{sep} = 26.6$. The separation bubble in case II has its maximum thickness of $\Delta y/S = 1.1$ at about 51% of the separation bubble length. In case III, the maximum separation bubble thickness of $\Delta y/S = 2$ is located at approx. 58% of the separation length.

Figure 7 shows the contours of the normalized Reynolds shear stress $\overline{u'v'}/u_0^2$ for all three cases. The shear layer downstream of the nozzle is affected by the expansion waves and the recompression shock emanating from the nozzle lip. In the reference case without shock interaction (Fig. 7a), the shear layer shows an undisturbed development downstream of $x/S \approx 7$, where the reflected recompression shock penetrates through the shear layer. Non-zero values of the Reynolds shear stress near the bottom wall indicate the formation of a turbulent boundary layer. As shown by Marquardt *et al.* (2016*b*), the transition of the boundary layer is triggered by the recompression shock emanating from the nozzle lip.

Both cases with shock interaction show turbulent mixing which is increased significantly compared to the reference case. A local increase in the Reynolds shear stress appears in the boundary layer on the bottom wall about $1.5S$ upstream of the separation point, where the reflected shock is formed. When the reflected shock passes through the shear layer and deflects the flow upwards, the Reynolds shears stress shows a strong local peak at the penetration point and remains increased by a factor of approx. 1.8 further downstream.

The highly unsteady separation leads to strong turbulent mixing on top of the separation bubble. Thus, the peak Reynolds shear stress is initially located closer the wall in case II, where the separation bubble is smaller. In case II, the shear layer is convected

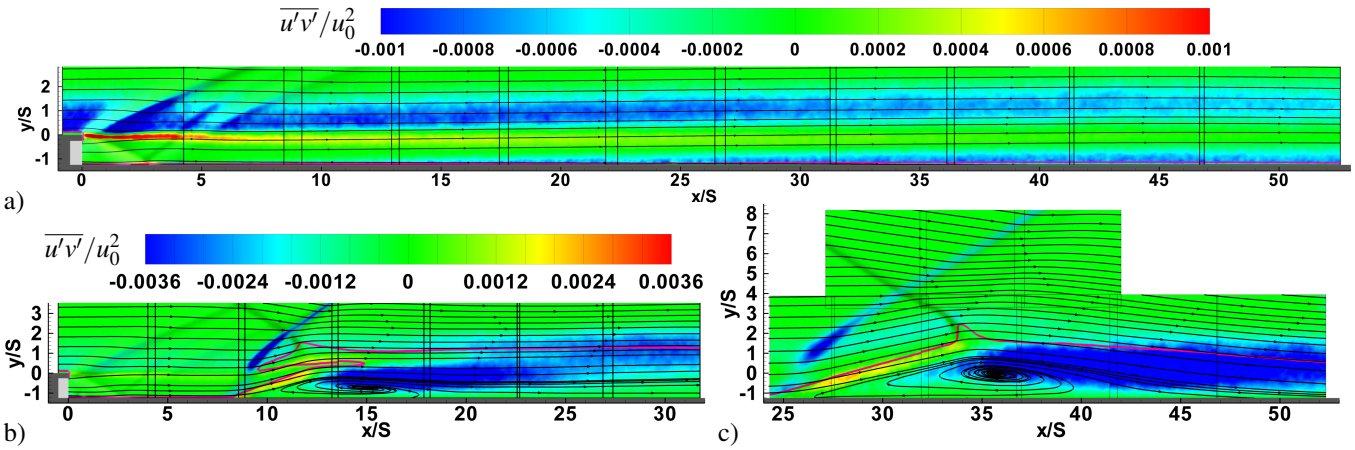

Figure 7. Contours of the normalized Reynolds shear stress $\overline{u'v'}/u_0^2$ for case I without shock interaction (a), for case II with shock interaction at $x_{imp}/S = 17$ (b), and for case III with shock interaction at $x_{imp}/S = 40$ (b). Plots (b) and (c) share the same color map. The synthetic schlieren image is superimposed to illustrate the positions of the shock and expansion waves.

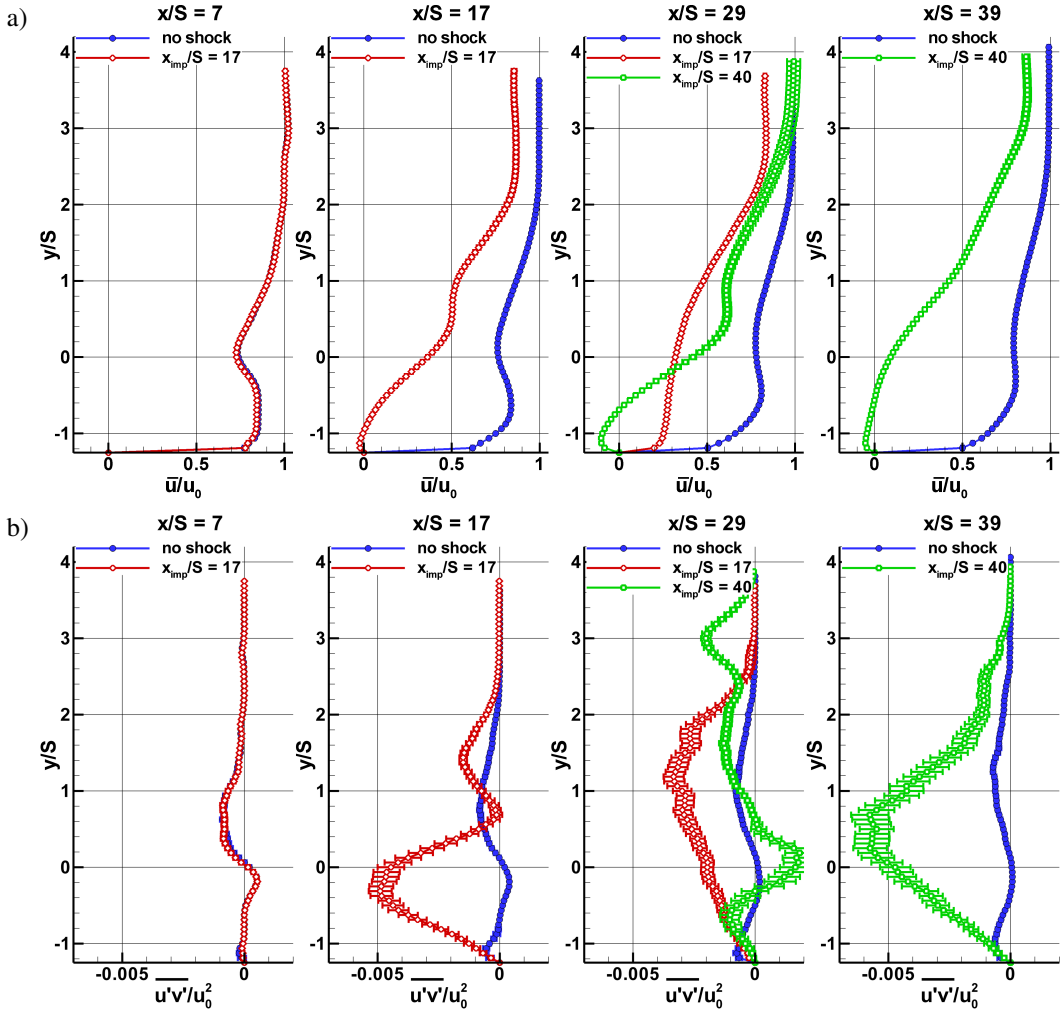

Figure 8. Profiles of the normalized mean streamwise velocity $\overline{u}/u_0$ (a) and the normalized Reynolds shear stress $\overline{u'v'}/u_0^2$ (b) for several streamwise positions x/S in the vicinity of the shock foot for all three cases. Due to the low measurement uncertainty, the error bars are covered by the symbols in some cases.

approximately parallel to the wall downstream of the point of maximum separation bubble thickness. Therefore, it does not merge with the highly turbulent zone originating from the separation bubble. Further downstream, i.e., where the boundary layer redevelops, the turbulent zone from the separation bubble decays, whereas the Reynolds shear stress in the shear layer increases. This leads to a single layer of increased turbulent mixing around $y/S = 1$ downstream of $x/S \approx 27$. In case III, the zone of high turbulent mixing at the top of the separation bubble is quickly convected towards the wall as the flow reattaches. This zone merges with the shear layer when it is deflected around the separation bubble and transported towards the wall again. Finally, this leads to the formation of a thick layer characterized by intense turbulent mixing ranging up to $y/S \approx 2$ which sustains further downstream.

Figure 8 shows the wall-normal profiles of the mean streamwise velocity $\overline{u}/u_0$ and the Reynolds shear stress $\overline{u'v'}/u_0^2$ for four streamwise positions x/S. The error bars in the plots include the statistic uncertainty of the measured quantity due to the finite amount of snapshots, random errors which arise from the used measurement techniques and sensors, as well as systematic errors introduced by the uncertainty of the reference velocity u_0 during normalization. To ensure repeatability of the measurements, several measurements conducted on different days were compared at the highly unsteady reattachment point of case II. The profiles of the normalized mean streamwise velocity $\overline{u}/u_0$ and the higher-order turbulence statistics, e.g., the normalized Reynolds shear stress $\overline{u'v'}/u_0^2$, of these measurements, match within the estimated error bounds.

Case II shows no upstream effect of the shock impingement on the profiles of the mean velocity $\overline{u}/u_0$ and the Reynolds shear stress $\overline{u'v'}/u_0^2$ at $x/S = 7$. The profiles of the cases without and with shock interaction coincide. The potential-core region, which is characterized by a uniform velocity distribution and the absence of Reynolds shear stress, extends over the range $-0.94 \leq y/S \leq -0.5$. Downstream of the shock impingement, i.e., at $x/S = 17$, backflow is apparent at $y/S < -1$ and the overall velocity decreases significantly. The upward shift of the shear layer leads to stronger mean velocity gradients in the shear layer and higher Reynolds shear stresses. The peak of the Reynolds shear stress profile is shifted about $\Delta y/S = 0.63$ off the wall compared to the undisturbed case. In the high intensity mixing zone downstream of the separation bubble, the normalized Reynolds shear stress reaches a level of $\overline{u'v'}/u_0^2 = -0.005$ at $y/S = -0.3$. At $x/S = 29$, the highly turbulent mixing zone has decayed and the Reynolds stress in the shear layer has increased. The boundary layer starts to redevelop with a Reynolds stress profile which peaks around $y/S = 1.2$ with a value of $\overline{u'v'}/u_0^2 = 0.0033$.

The large separation bubble in case III extends far upstream. Therefore, the velocity profile at $x/S = 29$, i.e., $\Delta x/S = 5$ up-

stream of the shock foot of case III, shows backflow in the range $y/S < -0.7$. Due to the flow deflection around the separation bubble, the shear layer has already been shifted off the wall at $x/S = 29$. Furthermore, even though the mean velocity profiles collapse in the range $y/S > 3.2$, the unsteady reflected shock causes an increased Reynolds shear stress which peaks at $y/S = 3.0$ with a value of $\overline{u'v'}/u_0^2 = -0.002$. At $x/S = 39$ and thus downstream of the shock impingement position of case III, the mean velocity profile still indicates the separation bubble by negative mean streamwise velocities in the range $y/S < -0.5$. Above the backflow area, the mean velocity is strongly decreased compared to the undisturbed case. However, the Reynolds shear stress is greatly increased downstream of the separation bubble, reaching values of $\overline{u'v'}/u_0^2 = -0.0057$ around $y/S = 0.5$. Further off the wall, i.e., in the range $y/S > 2$, the part of the shear layer that has not already merged with the mixing zone is apparent in the Reynolds shear stress profile.

Compared to the undisturbed reference case, both cases with shock interaction show a highly increased turbulent mixing downstream the impinging shock. This implies a higher transport of heat and momentum from the outer flow towards the wall. At a position $\Delta x/S = 5$ downstream the shock foot, the peak Reynolds shear stress in the mixing zone is increased by a factor of 6.0 in case II. When the flow recovers and the location of maximum Reynolds shear stress transitions to the shear layer at about $x/S = 29$, the Reynolds shear stress in the shear layer is higher by a factor of 4.2 compared to the undisturbed case. In case III, the peak Reynolds shear stress in the mixing zone is eight times higher than in the undisturbed case. When the boundary layer redevelops further downstream, the Reynolds shear stress is reduced to about the 6.4 fold of the reference case.

Conclusion

Supersonic slot-film cooling with and without shock impingement has been investigated using high-speed PIV measurements. A laminar cooling film is injected tangentially at an injection Mach number of $Ma_i = 1.8$ underneath a turbulent boundary layer at a freestream Mach number of $Ma_\infty = 2.45$. The inflow boundary layer has a thickness of 2.0 nozzle heights at the point of injection. Two cases with shock interaction and an undisturbed reference case are considered. A shock wave, generated by a wedge with $\beta = 8$ deg, impinges upon the cooling film either 17 or 40 nozzle heights downstream of the injection point, hence, either in the potential-core region or the wall-jet region.

An impinging shock induces severe separation of the cooling film and a pronounced unsteady separation bubble is formed which causes intense turbulent mixing downstream the impingement. Shock interaction in the potential-core region leads to a separation bubble with a length of approx. 9 nozzle heights, whereas shock interaction in the wall-jet region increases the separated length to about 15 nozzle heights. On top of the separation bubble, a zone characterized by intense turbulent mixing is generated. Due to the different size of the separation bubble, the wall-normal distance of this zone differs. With shock interaction in the potential-core region, the turbulent mixing zone is located beneath the shear layer downstream of the separation bubble. In this case the turbulent mixing decays quickly whereas the Reynolds shear stress in the shear layer increases further downstream. When the shock impinges in the wall-jet region, the highly turbulent mixing zone is located further off the wall and merges with the shear layer when the flow reattaches downstream of the separation bubble. The turbulent transport downstream of the impinging shock is increased up to a factor of 6.0 with shock interaction in the potential-core region and by a factor of 8.0 with shock impingement in the wall-jet region.

Acknowledgement

This research is funded by the Deutsche Forschungsgemeinschaft within the research project “Experimental Investigation of Turbulent Supersonic Film-Cooling Flows” (SCHR 309/62-1).

REFERENCES

Juhany, K. & Hunt, M. 1994 Flowfield measurements in supersonic film cooling including the effect of shock-wave interaction. *AIAA J* **32** (3), 578–585.

Konopka, M., Meinke, M. & Schröder, W. 2012 Large-eddy simulation of shock-cooling-film interaction. *AIAA J* **50** (10), 2102–2114.

Konopka, M., Meinke, M. & Schröder, W. 2013 Large-eddy simulation of shock-cooling-film interaction at helium and hydrogen injection. *Phys Fluids* **25** (10), 106101.

Marquardt, P., Klaas, M. & Michaux, F. 2016*a* PIV measurements of supersonic slot-film cooling with shock/cooling-film interaction. In *18th International Symposium on the Application of Laser and Imaging Techniques to Fluid Dynamics*. Lisbon, Portugal.

Marquardt, P., Klaas, M. & Schröder, W. 2016*b* PIV measurements of slot-film cooling at shock interaction. In *Fachtagung Experimentelle Strömungsmechanik*. Cottbus.

Pirozzoli, S. & Bernardini, M. 2011 Turbulence in supersonic boundary layers at moderate Reynolds number. *J Fluid Mech* **688**, 120–168.

Pirozzoli, S. & Bernardini, M. 2013 Probing high-Reynolds-number effects in numerical boundary layers. *Phys Fluids* **25** (2), 021704.

Seban, R. A. & Back, L. H. 1962 Velocity and temperature profiles in turbulent boundary layers with tangential injection. *J Heat Transfer* **84**, 45–54.